Supporting Information

Verification of the BCC Crystal Structure

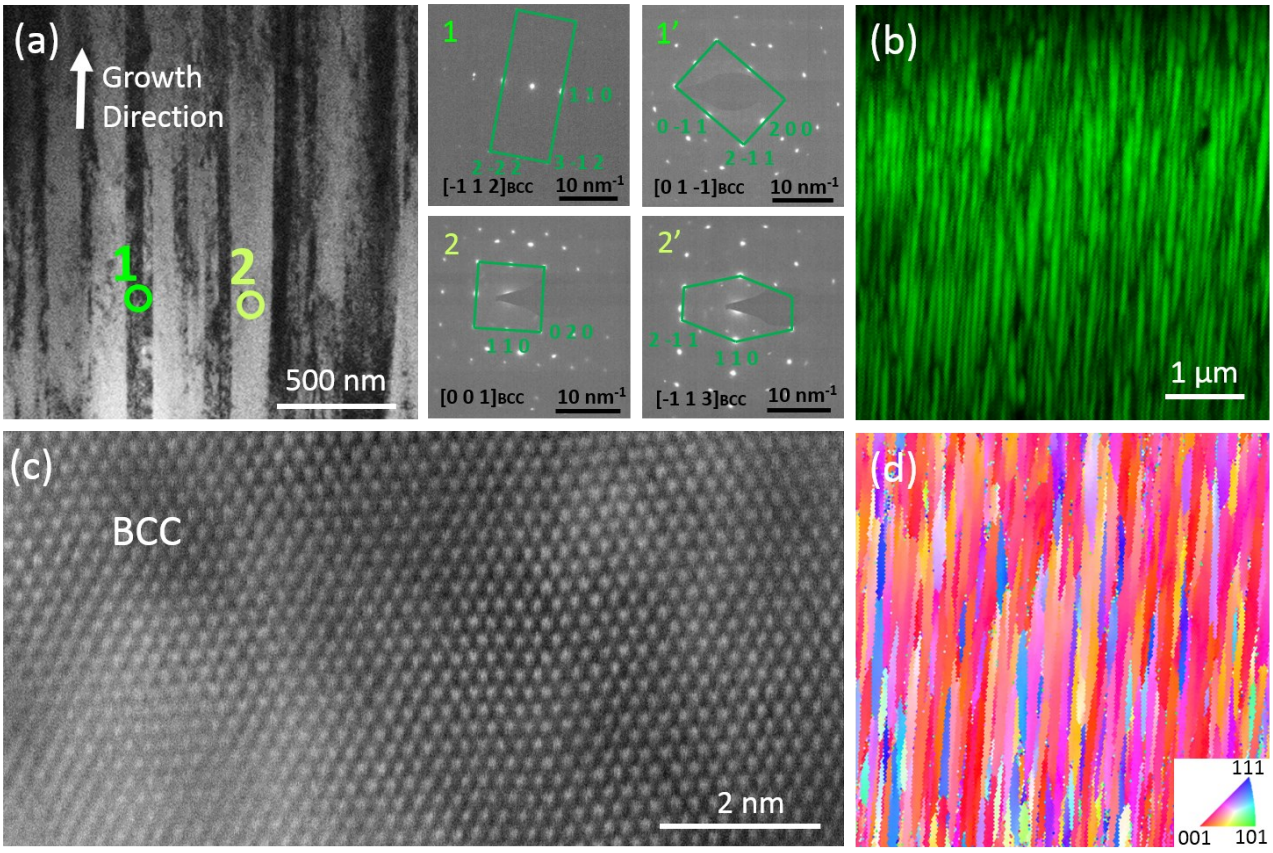

Figure S 1: (a) bright-field transmission electron microscope image showing columnar grain structure showing the grains in which diffraction patterns 1 and 2 where collected. Diffraction patterns 1' and 2' were collected from the same grains, but at different tilts; (b) EBSD results, where the colour green is indexed to the BCC phase, and (d) the corresponding Inverse Pole Figure map; (c) a typical STEM image showing the BCC structure along the [-1 1 1] zone axis.

To verify the crystal structure as BCC (in conjunction with TKD and EBSD data), a series of diffraction patterns were collected and indexed. In Figure S 1a, diffraction patterns 2 and 2', indexed as $[0\,0\,1]_{BCC}$ and $[-1\,1\,3]_{BCC}$ were collected at α tilts of $-29.24°$ and $-4.42°$, respectively, with the β tilt being held constant. The absolute difference in angles between these two patterns is $|(-29.24)-(-4.42)| = 24.82°$.

The angle between two vectors is given by;

$$cos\theta = \frac{\tilde{a}\cdot b}{\|a\|\|b\|}$$

Thus,

$$\theta = \cos^{-1}\frac{[0\ 0\ 1]\cdot[-1\ 1\ 3]}{\sqrt{0^2+0^2+1^2}*\sqrt{(-1)^2+1^2+3^2}} \approx 25.2°$$

Hence, as the theoretical (25.2°) and experimental ($24.8°$) values are in close agreement with each other, this provides additional confirmation that the crystal structure is BCC.

Calculation of the Lattice Parameter

The lattice parameter of BCC was calculated using XRD data. First, the interplanar spacing, *d*, can be determined via Braggs Law in equation 1, viz.

$$2d\sin\theta = n\lambda \qquad 1$$

Here, θ is the angle of diffraction, *n* is the order of reflection, and λ is the wavelength of the incident x-ray, viz. $1.7889 \times 10^{-10}\ m$. The major peak in the XRD data is the $(1\ 1\ 0)_{BCC}$ reflection occurring at 2θ = 52.2°, thus yielding;

$$d = \frac{n\lambda}{2sin\theta} = \frac{(1)(1.7889 \times 10^{-10}\ m)}{2\sin\left(\frac{52.2}{2}\right)} \approx 2.033 \times 10^{-10}\ m$$

Then, equation 2 is applied to obtain the lattice parameter.

$$d_{hkl} = \frac{a}{\sqrt{h^2+k^2+l^2}} \qquad 2$$

Here, d_{hkl} is the interplanar spacing with corresponding *h, k*, and *l* Miller indices, and *a* is the lattice parameter.

$$a = d_{hkl}\sqrt{h^2+k^2+l^2} = \left(2.033 \times 10^{-10}\ m\right)\left(\sqrt{1^2+1^2+0^2}\right) \approx 0.288\ nm$$

This value was subsequently used to calculate the atomic radius, which was used to determine the corresponding lattice parameters of FCC and HCP. These calculated lattice parameters were used to create block files used in the diffraction mapping; further details of which are available in the Experimental section.

Supplementary APT Data

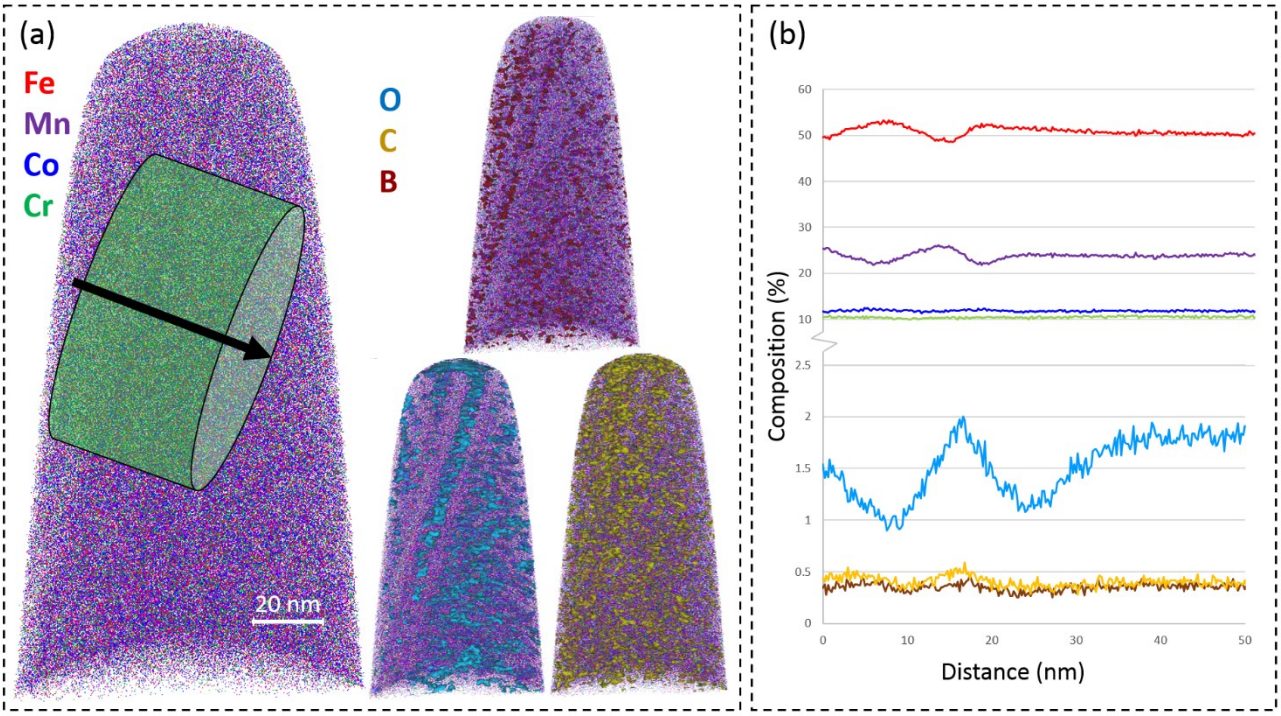

Figure S 2: (a) additional atom probe tomography reconstruction (left) showing Fe, Mn, Co and Cr, with B (0.8% threshold), C (1.0% threshold) and O (3.0% threshold) isosurfaces (right), and (b) 1D concentration line profiles displaying elemental segregation along the grain boundary (GB) along the arrow integrating over the cylinder cross section. Here, the inverse relationship between iron and manganese is more prominent.

Nanoindentation Load-Displacement Curves

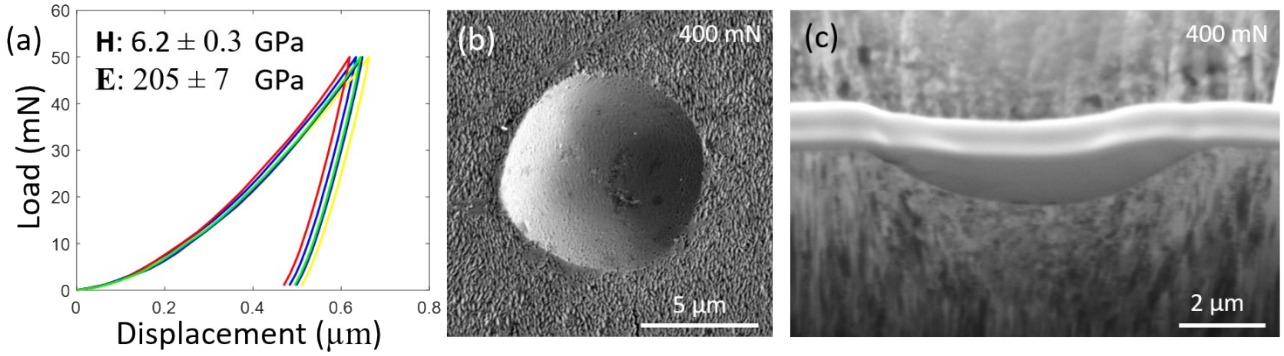

Figure S 3: (a) Load-displacement curves of the iHEA sample under a load of 50 mN (five data sets out of twenty shown) with the averaged hardness and Young's modulus indicated, (b) SEM image of spherical indentation impression on the surface and (c) cross-section of the indent imaged during FIB milling.

BCC || HCP Orientation Relationship

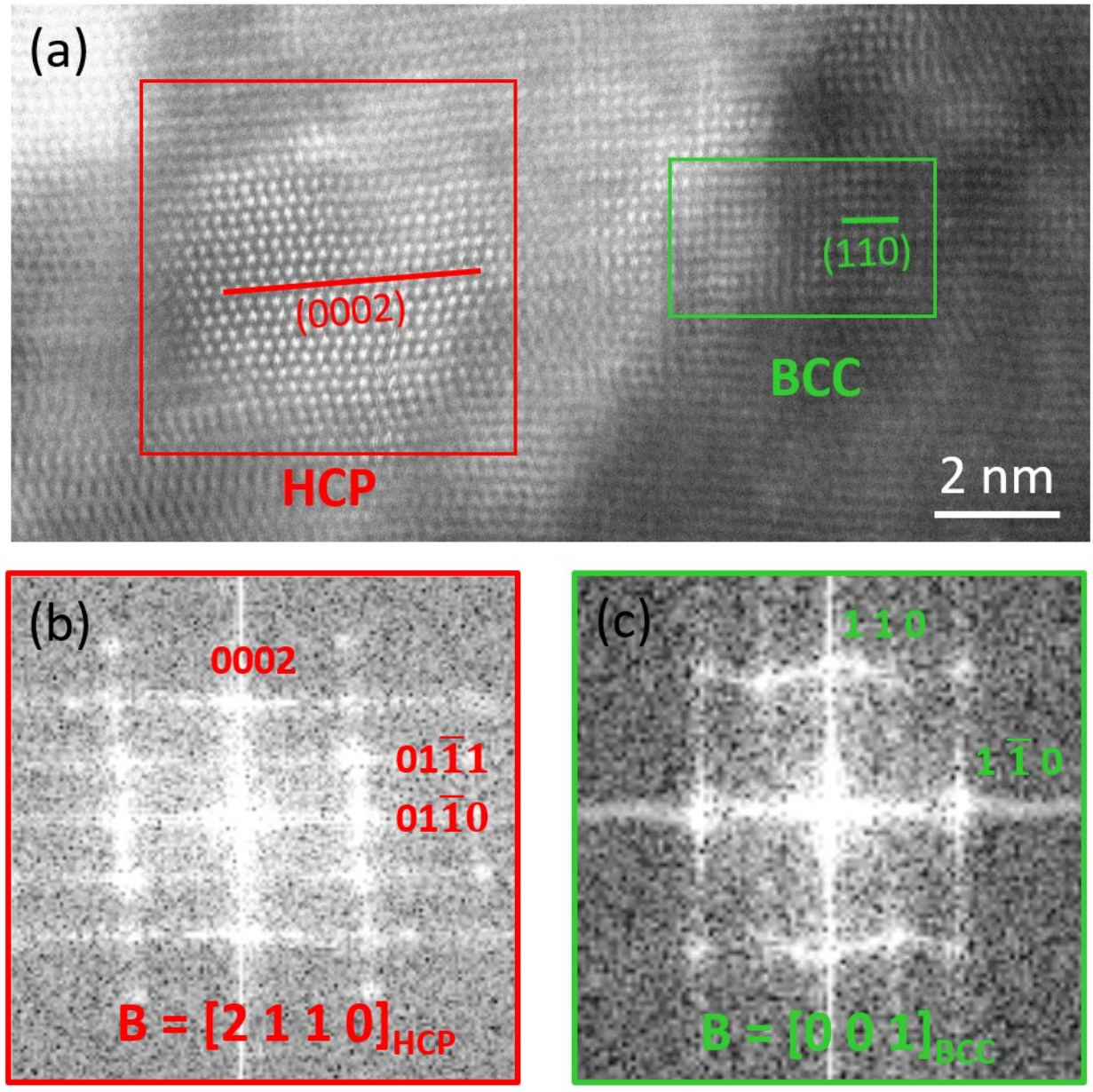

Figure S 4: $[2\bar{1}\bar{1}0]_{HCP}||[001]_{BCC}$ *orientation relationship between BCC and HCP; (a) STEM imaging showing respective regions, and (b) & (c) FFT from selected representative regions with the indicated zone axis, B.*

Mechanical Property Data

Table 1: Summary of mechanical property data for selected high-strength HEAs used to generate Figure 6.

Alloy Composition	Strain	Strength	Source
AlNbTiV	5.0	1020	[63]
NbMoTaWV	1.7	1246	[64]
TiZrNbTaMo	6.0	1390	[65]
$NbCrMo_{0.5}Ta_{0.5}TiZr$	5.0	1595	[66]
HfMoNbTaTiZr	10.0	1512	[67]
NbMoTaWVTi	10.6	1515	[68]
NbMoTaWTi	14.1	1343	[68]
WNbMoTaV	8.8	2612	[69]
NbMoTaWVCr	5.3	3416	[70]
TiVNbHf	16.1	1004	[28]
$Ti_{38}V_{15}Nb_{23}Hf_{24}$	22.5	802	[28]
$Ni_{43.9}Co_{22.4}Fe_{8.8}Al_{10.7}Ti_{11.7}B_{2.5}$	25	1040	[71]
CoCrFeMnNi	1.1	1210	[72]
$Al_{0.3}CoCrFeNi$	5.0	1800	[73]
NbTaTiV	23	1370	[74]
$Fe_{40}Co_{40}Ni_{10}Si_{10}$	38.3	1100	[75]
$Fe_{51.2}Mn_{24.3}Co_{11.9}Cr_{10.1}O_{1.4}C_{0.3}B_{0.2}$	28.9	2500	This Work

References

63. N. D. Stepanov, D. G. Shaysultanov, G. A. Salishchev and M. A. Tikhonovsky, Structure and mechanical properties of a light-weight AlNbTiV high entropy alloy, *Mater. Lett.*, 2015, **142**, 153–155.

64. O. N. Senkov, G. B. Wilks, J. M. Scott and D. B. Miracle, Mechanical properties of Nb25Mo25Ta25W25 and V20Nb20Mo20Ta20W20 refractory high entropy alloys, *Intermetallics*, 2011, **19**, 698–706.

65. S.-P. Wang and J. Xu, TiZrNbTaMo high-entropy alloy designed for orthopedic implants: As-cast microstructure and mechanical properties, *Mater. Sci. Eng., C*, 2017, **73**, 80–89.

66. O. N. Senkov and C. F. Woodward, Microstructure and properties of a refractory NbCrMo0.5Ta0.5TiZr alloy, *Mater. Sci. Eng., A*, 2011, **529**, 311–320.

67. C.-C. Juan, M.-H. Tsai, C.-W. Tsai, C.-M. Lin, W.-R. Wang, C.-C. Yang, S.-K. Chen, S.-J. Lin and J.-W. Yeh, Enhanced mechanical properties of HfMoTaTiZr and HfMoNbTaTiZr refractory high-entropy alloys, *Intermetallics*, 2015, **62**, 76–83.

68. Z. D. Han, N. Chen, S. F. Zhao, L. W. Fan, G. N. Yang, Y. Shao and K. F. Yao, Effect of Ti additions on mechanical properties of NbMoTaW and VNbMoTaW refractory high entropy alloys, *Intermetallics*, 2017, **84**, 153–157.

69. B. Kang, J. Lee, H. J. Ryu and S. H. Hong, Ultra-high strength WNbMoTaV high-entropy alloys with fine grain structure fabricated by powder metallurgical process, *Mater. Sci. Eng., A*, 2018, **712**, 616–624.

70. Y. Long, X. Liang, K. Su, H. Peng and X. Li, A fine-grained NbMoTaWVCr refractory high-entropy alloy with ultra-high strength: Microstructural evolution and mechanical properties, *J. Alloys Compd.*, 2019, **780**, 607–617.

71. T. Yang, Y. L. Zhao, W. P. Li, C. Y. Yu, J. H. Luan, D. Y. Lin, L. Fan, Z. B. Jiao, W. H. Liu, X. J. Liu, J. J. Kai, J. C. Huang and C. T. Liu, Ultrahigh-strength and ductile superlattice alloys with nanoscale disordered interfaces, *Science*, 2020, **369**, 427.

72. S. J. Sun, Y. Z. Tian, H. R. Lin, H. J. Yang, X. G. Dong, Y. H. Wang and Z. F. Zhang, Achieving high ductility in the 1.7 GPa grade CoCrFeMnNi high-entropy alloy at 77 K, *Mater. Sci. Eng., A*, 2019, **740–741**, 336–341.

73. B. Gwalani, S. Gorsse, D. Choudhuri, Y. Zheng, R. S. Mishra and R. Banerjee, Tensile yield strength of a single bulk Al0.3CoCrFeNi high entropy alloy can be tuned from 160 MPa to 1800 MPa, *Scr. Mater.*, 2019, **162**, 18–23.

74. W. Guo, B. Liu, Y. Liu, T. Li, A. Fu, Q. Fang and Y. Nie, Microstructures and mechanical properties of ductile NbTaTiV refractory high entropy alloy prepared by powder metallurgy, *J. Alloys Compd.*, 2019, **776**, 428–436.

75. C. Chen, Y. Fan, H. Zhang, J. Hou, W. Zhang, P. Wei, W. Wang, J. Qin, R. Wei, T. Wang and F. Li, A novel Fe-Co-Ni-Si high entropy alloy with high yield strength, saturated magnetization and Curie temperature, *Mater. Lett.*, 2020, **281**, 128653.